Kinetics and Mechanistic Aspects of the Oxygen Evolution Reaction at Hydrous Iron Oxide Films in Base

R. L. Doyle and M. E. G. Lyons

Email alerting service	Receive free email alerts when new articles cite this article - sign up in the box at the top right corner of the article or click here

Kinetics and Mechanistic Aspects of the Oxygen Evolution Reaction at Hydrous Iron Oxide Films in Base

R. L. Doyle[z] and M. E. G. Lyons

Trinity Electrochemistry Energy Conversion and Electrocatalysis (TEECE) Group, School of Chemistry & CRANN, Trinity College Dublin, Dublin 2, Ireland

The oxygen evolution reaction at multi-cycled iron oxy-hydroxide films in aqueous alkaline solution is discussed. The factors affecting the growth and electrocatalytic properties of the latter are described. In particular, steady-state Tafel plot analysis and electrochemical impedance spectroscopy have been used to elucidate the kinetics and mechanism of oxygen evolution. Tafel slopes of ca. 60 mV dec^{-1} and 40 mV dec^{-1} are found at low overpotentials depending on the oxide growth conditions, with an apparent Tafel slope of ca. 120 mV dec^{-1} at high overpotentials. Reaction orders of ca. 0.5, 1.0 and 1.5 are observed at low and high overpotentials, again depending on the oxide growth conditions. A mechanistic scheme involving the active participation of octahedrally coordinated anionic iron oxyhydroxide surfaquo complexes, which form the porous hydrous layer, is proposed. The latter structure contains considerable quantities of water molecules which facilitate hydroxide ion discharge at the metal site during active oxygen evolution. This work brings together current research in both heterogeneous electrocatalysis and homogeneous molecular catalysis for water oxidation.

Alkaline water electrolysis has been proposed as an environmentally inoffensive route to the production of the large volumes of hydrogen gas required by a possible hydrogen economy.[1–5] In practice, the efficiency of water electrolysis is limited by the large anodic overpotential of the oxygen evolution reaction (OER).[5] Over the past thirty years, considerable research effort has been devoted to the design, synthesis and characterization of OER anode materials, with the aim of achieving useful rates of active oxygen evolution at the lowest possible overpotential, in order to optimize the overall electrolysis process. Currently, the optimal OER anode materials are RuO_2 and IrO_2, since these oxides exhibit the lowest overpotentials for the OER at practical current densities.[6] However, the high cost of these materials and their poor long term stability in alkaline solution renders their widespread commercial utilization both uneconomical and impractical.[7] In light of these limitations, the oxides of the first row transition metals offer a compromise solution. Although they possess inferior electrocatalytic activity for the OER, their relatively low cost and long term corrosion resistance in alkaline solution makes them attractive OER anode materials.[7–12]

Despite this revival of interest the mechanism of the OER at first row transition metal oxide surfaces remains controversial and the question of a possible common mechanism, which would facilitate a theory of electrocatalysis for oxygen evolution, is therefore unresolved. It is our opinion that a systematic and consistent study of the OER at the oxidized surfaces of electrodes of adjacent first row transition metals should prove useful in elucidating whether a common reaction mechanism prevails.

In the present paper, we focus on the oxygen evolution electrocatalytic behavior of oxidized iron electrodes in alkaline solution. At present a number of studies exist concerning the OER at various iron containing electrodes including intermetallic alloys,[13,14] various mixed oxides[15–18] and hematite photoanodes[19–21] to name but a few. However, to the best of our knowledge, the work of Lyons et al.[10,11,22–25] and an early comparative study by Scarr[26] are the only meaningful studies on the kinetics of the OER at oxidized iron substrates. Here, we examine the OER kinetics at polymeric iron oxyhydroxide electrodes using a combination of steady state polarization techniques, reaction order studies and electrochemical impedance spectroscopy (EIS). The latter materials can be simply and reproducibly produced using a potential multicycling method and in the current work we highlight the most important factors influencing both their preparation and electrocatalytic properties. Finally, we propose a mechanism for the OER which specifically takes into account the

nature of the electrochemically generated hydrous iron oxide film present on the surface of the iron electrode during active oxygen evolution. Significantly, this mechanism, which is inspired by the classic work of Kobussen and Broers,[27] incorporates current thinking in both heterogeneous and homogeneous OER catalysis.

Experimental

All experiments were conducted in a conventional three electrode cell. The working electrode was constructed from 1.0 mm thick polycrystalline iron foil (as supplied by Alfa Aesar-Johnson Matthey, purity 99.9945% (metals basis)) with a geometric surface area of 0.16 cm^2. Prior to each experiment the surface of the working electrode was polished successively with 1200 grit carbimet paper and a slurry of 0.3 μm alumina powder until a "mirror bright" finish was achieved. A platinum wire electrode (CH Instruments, cat no. CHI 115) was employed as the counter electrode and a mercury-mercuric oxide (Hg/HgO) reference electrode (CH Instruments, cat no. CHI 152) was utilized as the reference standard, therefore all voltages are quoted against this reference electrode. The various electrolyte solutions were prepared from sodium hydroxide pellets (Sigma-Aldrich, minimum 99.0% purity), boric acid (BDH, minimum 99.5% purity) and sodium sulfate (Sigma-Aldrich, minimum 99.0% purity) using Millipore water (resistivity > 15 MΩ cm). Aqueous NaOH solutions served as both the electropolymerization medium and the primary supporting electrolyte for the redox switching and electrocatalytic studies. Borate buffer solutions acted as the supporting electrolyte for the pH experiments. These solutions contained 0.25 mol dm^{-3} boric acid and were made up to the appropriate pH using a 5.0 mol dm^{-3} NaOH solution. The ionic strength of each buffer solution was fixed at ca. 3.0 mol dm^{-3} using 1.0 mol dm^{-3} Na$_2$SO$_4$. Before commencing each experiment, nitrogen gas was bubbled through the electrolyte solution for 20 min.

The electrochemical measurements, with the exception of the impedance measurements, were performed using a range of high performance potentiostats including a CHI760D bipotentiostat, an Autolab PGSTAT302N potentiostat/galvanostat, and Gamry Reference 3000 and 600 potentiostat/galvanostat/ZRA systems. Unless otherwise specified, all values of current density are normalized with respect to the geometric surface area of the electrode. Tafel plots were recorded using linear sweep voltammetry which was performed at a sweep rate of 1 mV s^{-1} in the positive direction. Each Tafel plot was corrected for *iR* drop. Accordingly, the uncompensated solution resistance was determined using chronoamperometry. The current response to a small potential step (50 mV) was recorded in a potential region where no faradaic processes were occurring. The solution

resistance was then calculated using the relationship,

$$i = \frac{\Delta E}{R} \exp\left(\frac{-t}{R_u C_{dl}}\right) \qquad [1]$$

where ΔE is the magnitude of the potential step (V), R_u is the uncompensated solution resistance (ca. 0.4 Ω for 1.0 mol dm^{-3} NaOH), t is time (s) and C_{dl} is the double layer capacitance (F). Electrochemical impedance spectroscopy was performed using a Zahner Elektrik IM6 electrochemical measurement unit. The impedance spectra were recorded by employing a 10 mV peak to peak amplitude sine wave potential perturbation on the dc potential. The dc potential was changed step wise in the positive direction, with sufficiently long delays to achieve steady state conditions. This has been checked by applying Kramers–Kronig tests to the measured spectra. Complex non-linear least squares (CNLS) fitting of raw impedance data to equivalent circuit models was conducted using the SIM module of the IM6 Thales software suite.

The polymeric iron oxyhydroxide films were prepared by multi-cycling a polycrystalline iron electrode in the requisite electrolyte solution between appropriate switching potentials. The aforementioned experimental parameters have been varied in this work and so the pertinent values are noted in the relevant results sections. Films of different thicknesses were prepared by varying the number of growth cycles in the multi-cycling procedure. The charge storage capacity or redox capacity (Q) was determined following the growth of each film by integrating the peaks in a voltammetric profile recorded at a slow sweep rate (40 mV s^{-1}). The redox capacity is directly proportional to the thickness of the layer.

Results and Discussion

Preparation and redox characteristics of polymeric hydrous iron oxide.— Polymeric hydrous iron oxide films have been prepared *via* the potential multi-cycling technique outlined above. In this method the potential of an electrode of the parent metal (which may be noble or non-noble) is cycled repetitively between suitable lower and upper limits in an aqueous solution of appropriate pH. The type of potential perturbation used for oxide growth – sinusoidal, square or triangular wave- apparently makes little difference. Indeed, the triangular wave is most convenient as changes in the current vs. potential response (the voltammogram) can be employed during the oxide growth reaction to monitor changes in redox behavior associated with the latter.

Typical cyclic voltammograms recorded for hydrous oxide layers prepared using different numbers of growth cycles are presented in Fig. 1a. The surface redox chemistry of a polycrystalline iron electrode

in base has been discussed in detail by Lyons and coworkers[11,22,28] and in the present article we adopt the peak designations adopted by these authors. It is clear from Fig. 1a that the A3/C2 peaks are the only peaks to display a significant enhancement upon potential cycling. In simple terms peaks A3/C2 can be attributed to the following Fe(II)/Fe(III) redox transformation,

$$Fe(OH)_2 + OH^- \rightarrow FeOOH + H_2O + e^- \qquad [2]$$

However, it was previously shown that the A3/C2 peaks exhibit the usual characteristic of a hydrous or hyper-extended oxide,[28] i.e. *a super-nernstian potential-pH shift*, which has the value of dE/dpH = $-2.303(3RT/2F) = -0.088$V/pH unit at T = 298 K. Accordingly, by analogy with a scheme produced by Burke and Whelan[29] for redox switching of iridium oxide films, it has been proposed that the main redox switching reaction may be written as,

$$[Fe_2(OH)_6(OH_2)_3]_n^{2-} + 3nOH^-$$

$$\rightarrow [Fe_2O_3(OH)_3(OH_2)_3]_n^{3-} + 3nH_2O + 2ne^- \qquad [3]$$
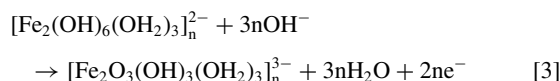
corresponding to an Fe(II)/Fe(III) redox transition in a polymeric microdispersed hydrous oxide layer. The oxide/solution interface of hydrous oxide films prepared in this way is thought to consist of an inner compact anhydrous layer MO$_x$ and an outer microdispersed hydrous layer of general form MO$_a$(OH)$_b$(OH$_2$)$_c$. This is the duplex layer model proposed by Burke and coworkers[30,31] and depicted graphically in Fig. 1b. In this model, the ions of the inner region are held in place by a rigid network of polar covalent bonds through which ionic transport is difficult whereas charge percolation proceeds comparatively easily and quickly through the outer, hydrous, polymeric oxide region. In fact, Lyons and Brandon[22] have recently shown that the rate of charge diffusion for a hydrous oxide covered Fe electrode in base is comparable to that of poly(pyrrole) with an average charge transport diffusion coefficient D_{CT} of ca. 3.0×10^{-10} cm^2 s^{-1}. On repetitive cycling, the porous outer layer increases in thickness at the expense of the underlying metal, the mechanism of which has been described by Burke and Lyons,[28] and Pickup and Birss.[32]

The extent of hydrous oxide growth is known to depend strongly on the values chosen for the upper and lower limit of the potential sweep as well as the cycling frequency, the solution temperature and the solution pH. However, of these various growth conditions the lower potential sweep limit is probably the most important. The variation in oxide charge capacity Q (determined by integration of the voltammetric peak A3) as a function of the lower potential limit is presented in Fig. 2a for hydrous oxide films prepared using 120 growth cycles in 0.5 and 1.0 mol dm^{-3} NaOH. A previously optimized sweep rate of 350 mV s^{-1} was employed.[28] It is clear from Fig. 2a that an optimum
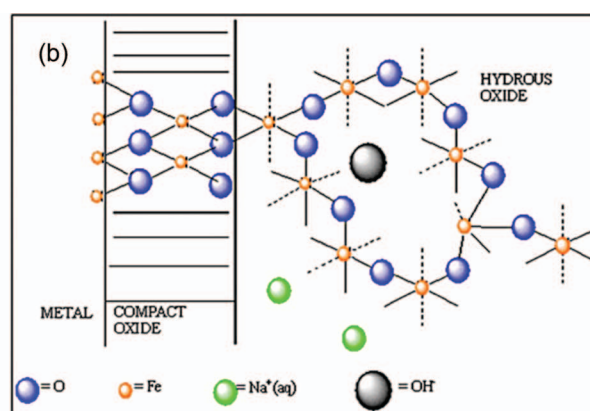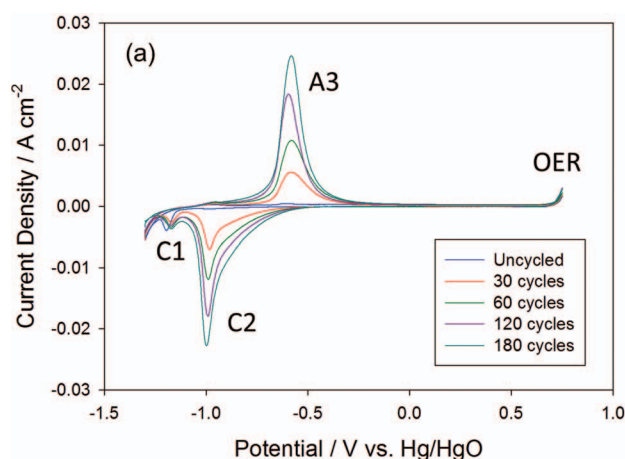
Figure 1. (a) Cyclic voltammograms recorded in 1.0 M NaOH at a sweep rate of 40 mV s^{-1} for hydrous iron oxide films prepared using a range of growth cycles. The films were grown in 0.5 M NaOH between switching potentials of -1.30 V and 0.75 V at a sweep rate of 400 mV s^{-1}. (b) Schematic representation of the Burke-O'Sullivan Duplex Layer Model of the oxide/solution interface.
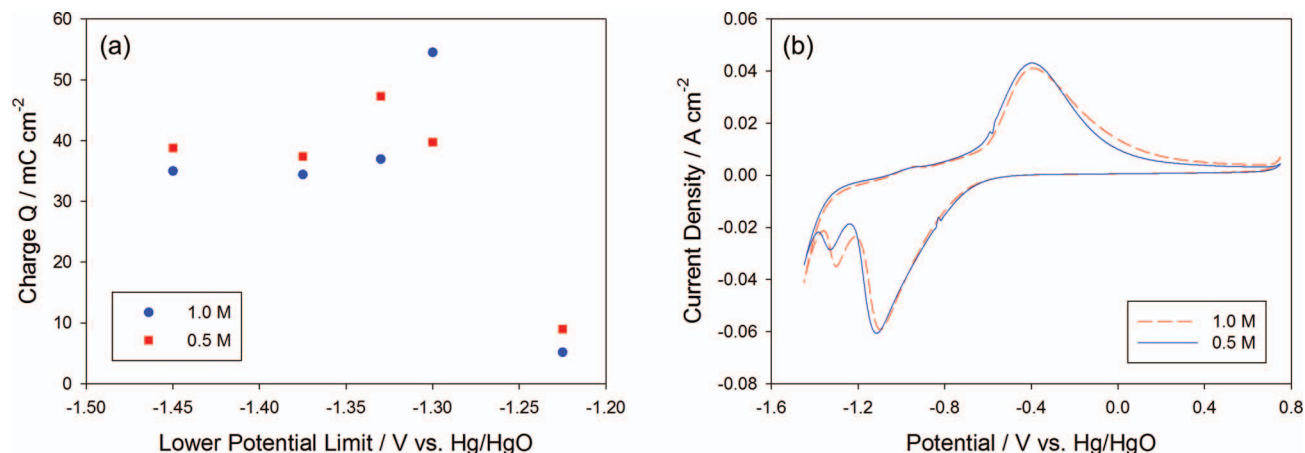
Figure 2. (a) The voltammetric charge capacity Q under the A3 peak plotted as a function of the lower potential limit for hydrous oxide films prepared using 120 growth cycles in 0.5 and 1.0 mol dm^{-3} NaOH with a fixed upper limit of 0.75 V and a sweep rate of 350 mV s^{-1}. (b) Typical cyclic voltammograms recorded during the growth of hydrous oxide films in 0.5 and 1.0 mol dm^{-3} NaOH between the switching potentials of -1.45 V and 0.75 V at a sweep rate of 350 mV s^{-1}.

lower limit exists for hydrous oxide growth with maximum Q values being obtained at -1.33 and -1.30 V respectively in 0.5 and 1.0 mol dm^{-3} NaOH. The significance of these optimum values can be readily understood by examining the voltammetric profiles recorded during hydrous oxide growth in each medium. In Fig. 2b representative cyclic voltammograms recorded during the growth of hydrous oxide films in 0.5 and 1.0 mol dm^{-3} NaOH are presented. It is interesting to note that the C1 peak potential observed in each medium, corresponding to the reduction of the compact anhydrous inner layer, is the same as the related lower limit from Fig. 2a. associated with the maximum oxide charge capacity. That is, the extent of hydrous oxide growth is greatest when the potential sweep is reversed at the C1 peak potential. Thus, the marked dependence of oxide growth rate on the lower limit of the potential sweep is indicative of the essential role that partial reduction of the anhydrous oxide plays in the production of a thick deposit. Partial reduction of the compact oxide layer apparently facilitates rearrangement of oxycation species at the metal surface, leaving it in a somewhat disrupted state. On subsequent re-oxidation of the partially reduced metal surface the compact layer is restored but the outer region of the compact film is present in a more dispersed form and on further reduction the latter material becomes incorporated into the hydrated outer layer.

The upper limit of the potential sweep also has an important effect on the rate of oxide growth. The effect of this parameter lies principally in the fact that the more anodic the value of the upper potential limit the more difficult the reduction of the compact anhydrous oxide layer becomes. This is illustrated clearly in Fig. 3a where cyclic voltammograms recorded during the growth of hydrous oxide films using a fixed lower potential limit of -1.30 V and upper potential limits of 0.35 and 0.75 V are shown. A clear shift of the C1 peak in the cathodic direction is evident as the upper potential limit is increased. This behavior is likely due to increased passivation of the electrode surface at the more anodic potentials. Consequently, a relationship exists between the upper and lower limit such that the optimal lower limit necessary to achieve maximum hydrous oxide growth is dependent on the value chosen for the upper limit of the potential sweep. Therefore, in order to truly examine the effect of the upper limit on hydrous oxide growth it was necessary to determine the optimum lower limit corresponding to each upper limit. Accordingly, the voltammetric charge capacity Q is plotted as a function of the upper potential limit in Fig. 3b for hydrous oxide films prepared in 0.5 and 1.0 mol dm^{-3} NaOH using 120 growth cycles where each corresponding lower limit had been optimized to coincide with the C1 peak potential. It can be seen from Fig. 3b that the efficiency of hydrous oxide growth increases
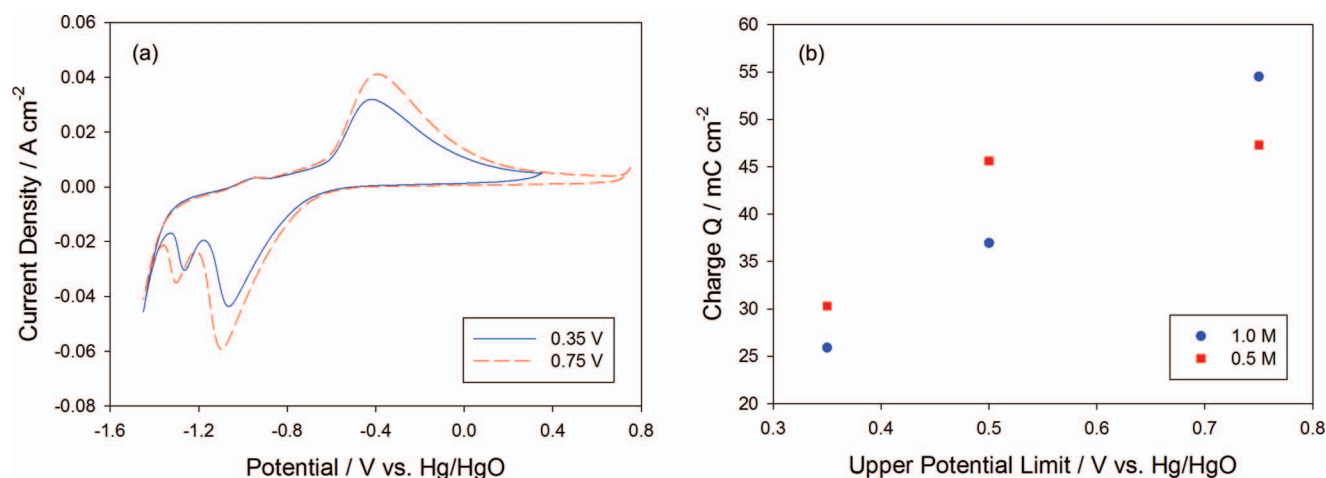

Figure 3. (a) Cyclic voltammograms recorded during the growth of hydrous oxide films in 1.0 mol dm^{-3} at a sweep rate 0f 350 mV s^{-1} between a fixed lower potential limit of -1.45 V and upper potential limits of 0.35 V and 0.75 V. (b) The voltammetric charge capacity Q under the A3 peak plotted as a function of the upper potential limit for hydrous oxide films prepared using 120 growth cycles in 0.5 and 1.0 mol dm^{-3} NaOH with optimized lower potential limits and a sweep rate of 350 mV s^{-1}.
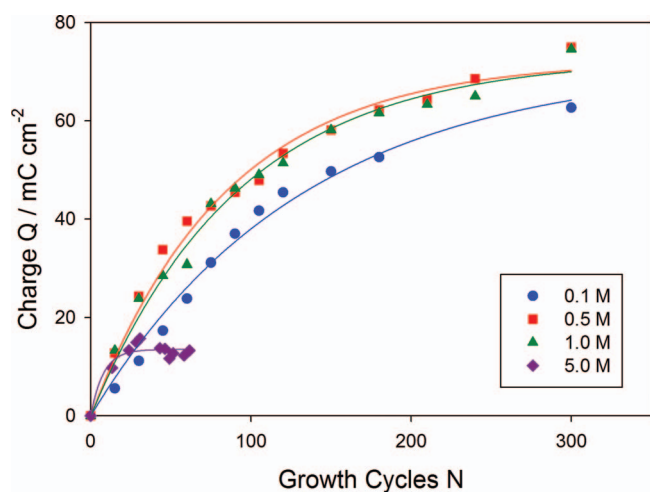
Figure 4. The voltammetric charge capacity Q under the A3 peak as a function of the number of optimized growth cycles N for hydrous oxide films prepared in 0.1, 0.5, 1.0 and 5.0 mol dm^{-3} NaOH. The growth curves simulated using eqn. 4 and fitting the data in Table I are shown as continuous lines.
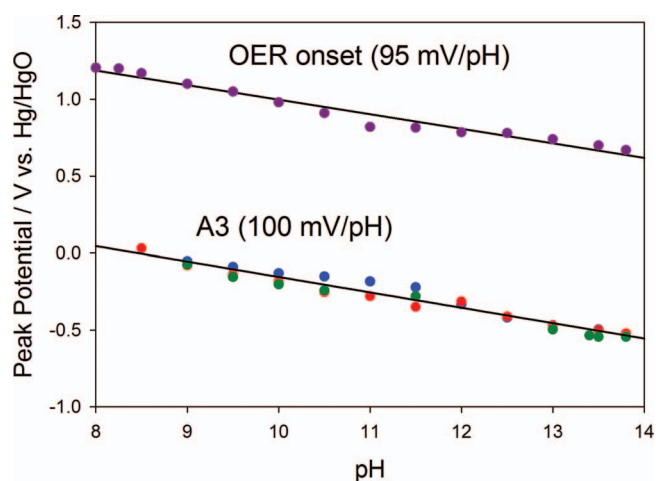

Figure 5. The A3 peak potential and the OER onset potential for a typical hydrous iron oxide covered electrode plotted as a function of the solution pH.

for more anodic upper potential limits. The importance of this parameter probably lies in the fact that it extends oxygen penetration into the outer regions of the metal lattice resulting in thickening of the compact layer. Indeed, it has been noted that the upper limit must be sufficiently anodic that compact oxide formation exceeds significantly the single monolayer level so that on subsequent reduction, a disturbed, highly disordered layer of metal atoms is prepared on the electrode surface thereby facilitating hydrous oxide growth.[33] Furthermore, employing more anodic upper potentials may help to generate a slight expansion and stress associated disruption at the metal-oxide interface and may also enable the uptake of a slight excess of oxygen by the oxide phase.

The effect of base concentration on the rate of hydrous oxide growth has also been examined. In light of the above discussion, optimized values for the upper and lower potential sweep limits were determined for a range of base concentrations. Subsequently, the growth of the hydrous oxide film using these optimum parameters was monitored by following the development of the redox capacity Q as a function of the number of cycles N. The resultant growth profiles generated in the various base concentrations are presented in Fig. 4. Experimentally, it was found that the charge tends toward a constant limiting value as N is increased and can be fitted using the simple expression,

$$Q = a[1 - \exp(-bN)] \quad [4]$$

The simulated growth curves are represented by continuous lines and the pertinent nonlinear least squares (NLLS) fitting parameters are included in Table I. The decrease in oxide growth rate dQ/dN with increasing film thickness can be attributed to the increasing inhibition of water and hydroxide ion transfer to the inner region of the oxide layer with increasing hydrous oxide thickness. Furthermore, it is apparent from Fig. 4 that the rate of hydrous oxide growth is dependent on the electrolyte concentration. During the initial stages of layer growth (small N), the growth rate is more rapid in the more concentrated (5.0 mol dm^{-3}) as opposed to the more dilute

(0.1 mol dm^{-3}) hydroxide solution. However the growth rate decreases quite rapidly with increasing N in the more concentrated medium, whereas the growth rate is less affected with increasing N in the more dilute solutions. Evidently, increased hydroxide ion activity suppresses hydroxide dissociation and /or favors adsorption of this species. This will result in the inhibition of crystallization of the hydrous oxide layer, and the resulting more amorphous film will be more effective in excluding water from the inner region of the oxide film, thereby inhibiting the growth of the microdispersed hydrous layer. Certainly, as can be seen from Fig. 4 and from the *a* values in Table I, significantly greater redox capacities may be obtained for hydrous oxide layers prepared in the lower base concentrations whereas only limited development of the hydrous layer can be achieved in very concentrated base, with inhibition of hydrous oxide growth becoming apparent after only 20–30 growth cycles in 5.0 mol dm^{-3} NaOH.

Finally, it has been noted that dispersed hydrated oxide materials exhibit good electrocatalytic potentiality due to their skeletal nature as the latter structural feature permits a major increase in the number of oxyions participating in the electrode reaction.[11,22] Indeed, with microdispersed species the boundary between the solid and aqueous phase may be nebulous as the two phases virtually intermingle. This will be an important consideration when a model for the OER is developed. In our mechanistic analysis we specifically implicate the hydrous layer as the catalytic species. This assertion is supported by the pH dependence of the OER at hydrous iron oxide covered electrodes. In Fig. 5, *E*-pH plots generated for peak A3 and the OER onset potential are presented for comparison. As stated previously, the redox peaks associated with the hydrous layer exhibit a supernernstian *E*-pH dependence, here A3 shifts negatively by ca. 0.1 V/pH unit. Significantly, the OER onset potential exhibits an *E*-pH shift of similar magnitude to peak A3, ca. −0.095 V/pH unit, suggesting that the anionic surfaquo groups of the hydrous layer actively partake in oxygen evolution at hydrous oxide covered iron electrodes.

Oxygen evolution reaction steady state polarization measurements.— Steady-state polarization curves were recorded for hydrous oxide films prepared using a range of base concentrations. Typical *iR* corrected Tafel plots for hydrous oxide films prepared in 0.5 and 1.0 mol dm^{-3} NaOH using increasing numbers of growth cycles are presented in Fig. 6. The steady-state polarization response of an uncycled Fe electrode is also presented in Fig. 6b for the purpose of comparison. It is immediately evident from Fig. 6 that the oxygen evolution performance of a multi-cycled Fe electrode is significantly enhanced relative to an uncycled electrode. The effect of multi-cycling the electrode is to increase the OER current and decrease the OER overpotential. This observation is in agreement

Table I. Nonlinear least squares fitting parameters for the data in Fig. 4 to eqn. 4.

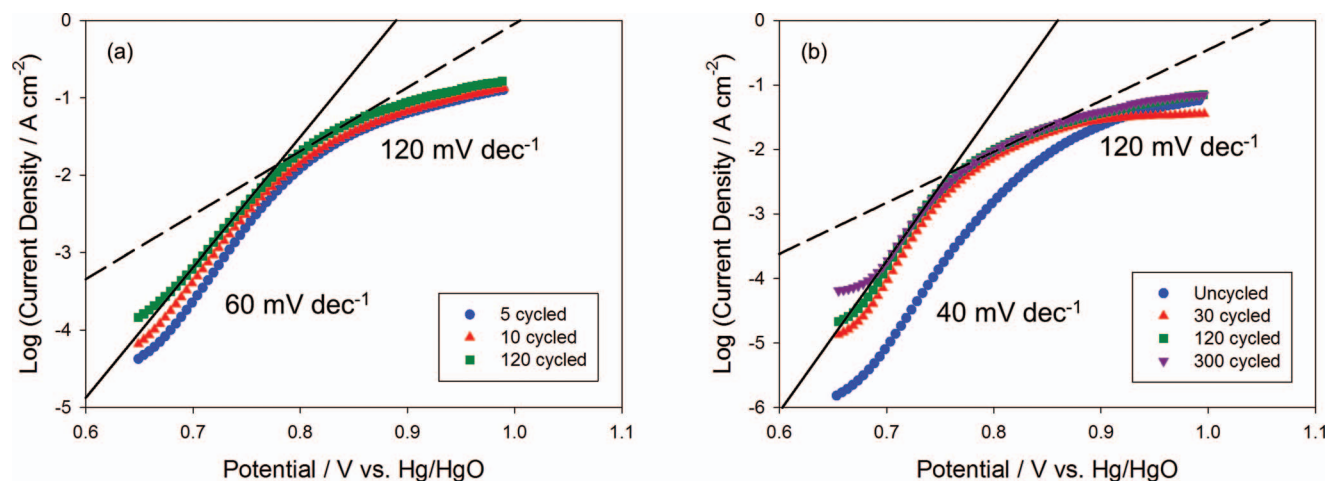| [OH$^-$] / mol dm^{-3}	a / mC	b / cycles^{-1}	R^2
0.1	71.6	0.008	0.988
0.5	72.4	0.012	0.986
1.0	72.8	0.011	0.987
5.0	13.5	0.128	0.907

Figure 6. Steady-state polarization curves recorded in 1.0 mol dm^{-3} NaOH for hydrous iron oxide films prepared using a range of growth cycles. The films were grown (a) in 1.0 mol dm^{-3} NaOH between switching potentials of -1.45 V and 0.35 V at a sweep rate of 350 mV s^{-1} and (b) in 0.5 mol dm^{-3} NaOH between switching potentials of -1.30 V and 0.75 V at a sweep rate of 400 mV s^{-1}.

with previous results reported by Lyons and coworkers[22–24] for a number of different multi-cycled iron electrodes. Indeed, it has been shown by Gennero De Chialvo and Chialvo[34,35] that the rate of the OER in aqueous alkaline solution is also enhanced for multi-cycled Ni and Co anodes relative to uncycled electrodes of the same metal, although these workers did not offer any mechanistic rationalization of their kinetic data.

A similar conclusion can be drawn from the data of Fig. 7, where the OER current density, recorded at a fixed potential $E = 0.70$ V vs. Hg/HgO, and the oxygen evolution potential, recorded at a fixed OER rate of 1.0 mA cm^{-2}, are plotted, respectively, as a function of the hydrous oxide charge capacity. It is noteworthy at this stage that the OER does not occur on a metallic surface in the case of the uncycled Fe electrode. Upon introduction to alkaline solution and application of an anodic polarization regime, a passive oxide will form on the metal surface, and it is at the surface of this oxide that electrocatalysis of the OER occurs. Therefore, the increase in oxygen evolution rate, manifested as increasing current density in Fig. 7a, with increasing oxide charge capacity suggests that the enhanced electrocatalytic activity of the multi-cycled electrodes is due to increasing real electrode area. That is, the oxide charge capacity is proportional to the mass of the film, which, for a microporous layer, is linearly related to the surface area. Furthermore, the system becomes more electrocatalytically efficient with increasing oxide charge capacity. In Fig. 7b the oxygen

evolution potential recorded at a fixed OER rate is seen to decrease significantly as the hydrous oxide charge capacity increases. Hence, the OER requires less driving force to achieve the same rate as the thickness of the hydrated layer increases.

The important kinetic feature evident in Fig. 6 is the variation in the Tafel characteristic with electropolymerisation solution. Dual Tafel slopes were exhibited by all the hydrous oxide films examined, with a Tafel slope b ca. 120 mV dec^{-1} ($\approx 2.303 \times 2RT/F$ at 25°C) uniformly observed at high overpotentials. However, at low overpotentials the Tafel slope was dependent on the base concentration used to prepare the film. When the concentration of NaOH was greater than or equal to 1.0 mol dm^{-3} b was ca. 60 mV dec^{-1} ($\approx 2.303 \times RT/F$ at 25°C) whereas for NaOH concentrations less than or equal to 0.5 mol dm^{-3} the Tafel slope b was ca. 40 mV dec^{-1} ($\approx 2.303 \times 2RT/3F$ at 25°C). These two distinct sets of Tafel slopes have been designated Type A and Type B respectively.[36]

The effect of solution OH$^-$ ion concentration on the rate and kinetics of the OER at these different hydrous oxide films was also investigated. For each experiment, the oxide layer was grown for the requisite number of cycles in the appropriate electropolymerisation solution and the electrode was then transferred to the test solution. A comparison of the steady state polarization curves obtained for 120 cycled hydrous oxide films in various base concentrations is presented in Fig. 8. It can be seen from each of the plots in Fig. 8 that the Tafel
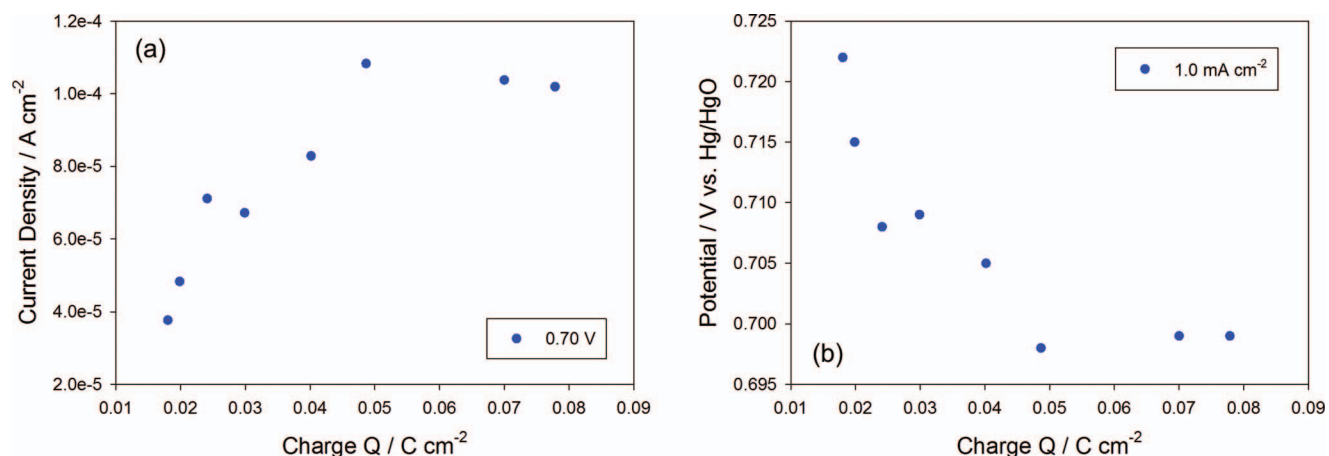

Figure 7. (a) The oxygen evolution current measured at 0.70 V and (b) the potential required to generate 1.0 mA cm^{-2} of OER current as a function of hydrous oxide charge capacity (Q).
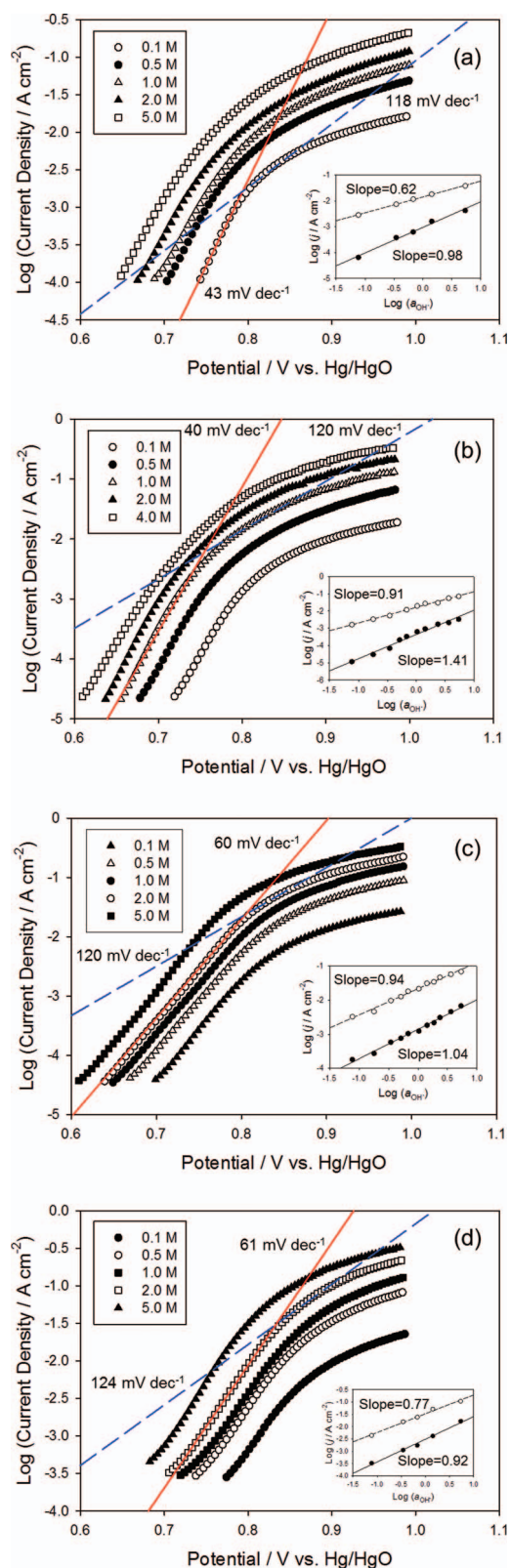
Figure 8. Steady-state polarization curves recorded in a series of base concentrations for hydrous iron oxide films prepared using 120 growth cycles. The films were grown (a) in 0.1 mol dm^{-3} NaOH between switching potentials of −1.33 V and 0.75 V at a sweep rate of 400 mV s^{-1}, (b) in 0.5 mol dm^{-3} NaOH between −1.30 V and 0.75 V at a sweep rate of 400 mV s^{-1}, (c) in 1.0 mol dm^{-3} NaOH between −1.45 V and 0.35 V at a sweep rate of 350 mV s^{-1} and (d) in 5.0 mol dm^{-3} NaOH between −1.38 V and 0.65 V at a sweep rate of 400 mV s^{-1}. Reaction order plots generated at fixed potentials in the low and high Tafel slope regions are shown in the insets of each graph.

characteristics for each film remain the same regardless of base concentration, suggesting that the nature of the rate determining step is unaffected by the concentration of OH$^-$ ions in solution. Again, Tafel slopes of ca. 60 and 40 mV dec^{-1} were observed at lower potentials for Type A and Type B films respectively, with a Tafel slope of approximately 120 mV dec^{-1} becoming evident at higher overpotentials. Reaction order plots with respect to OH$^-$ ion activity (calculated from literature values[37] for the mean ionic activity coefficients, $\gamma\pm$) are constructed in the insets of Fig. 8. As was observed for the Tafel slopes, the reaction orders mOH$^-$ were found to be dependent on the electropolymerisation solution. Reaction orders of 0.98, 1.41, 1.04 and 0.92 were obtained at potentials located in the low Tafel region for hydrous oxide films prepared in 0.1, 0.5, 1.0 and 5.0 mol dm^{-3} respectively. In the high Tafel region the corresponding reaction orders were 0.62, 0.91, 0.94 and 0.77 respectively. Similar numerical values for the reaction orders were obtained for hydrous oxide layers prepared using a range of growth cycles indicating that the reaction order is not dependent on the hydrous oxide charge capacity.

The results outlined above highlight a clear dependence of the hydrous oxide OER kinetic parameters on the electropolymerisation solution. We propose that this variation in the electrocatalytic properties associated with the hydrous oxide film is ultimately a dehydration or 'aging' effect. As outlined previously, the films prepared in the more concentration base solutions are thought to be less crystalline and more dehydrated than those prepared in the lower base concentrations. Thus, it is the increasing amorphous or dehydrated nature of the hydrous oxide films that is responsible for the changing electrocatalytic properties. To further illustrate this idea we investigated the effect of 'aging' on the Tafel characteristics of a hydrous oxide layer. 'Aging' in this sense refers to immersing a freshly prepared hydrous oxide covered electrode in 5.0 mol dm^{-3} NaOH for a prolonged period of time. In Fig. 9 a comparison of the Tafel plots recorded for a Type B hydrous oxide film in 5.0 mol dm^{-3} NaOH before (Fig. 9a) and after (Fig. 9b) 'aging' for 2 hours is presented. The lower Tafel slope was observed to increase from 44 mV dec^{-1} to 60 mV dec^{-1} with 'aging'. Dehydrating the layer in strong base effectively transformed it from a Type B hydrous oxide film into one exhibiting Type A behavior. In this way, we can attribute the variation in the OER kinetic parameters to changes in the level of crystallinity and hydration of the hydrous layer.

Electrochemical impedance spectroscopy (EIS).— Electrochemical impedance spectroscopy was employed to obtain a better understanding of the different OER kinetic properties being exhibited by the hydrous oxide films. With this in mind, the electrochemical impedance response of hydrous iron oxide covered electrodes was recorded over a range of potentials associated with active oxygen evolution. A series of impedance spectra recorded for a Type A and Type B hydrous oxide film, prepared using 120 growth cycles, are presented in the Nyquist and Bode format in Fig. 10. These spectra are representative of the impedance response of the different hydrous iron oxide films as a whole. The raw impedance data was fitted, using a CNLS fitting algorithm, to the equivalent circuit model depicted in Fig. 11 and the simulated data is presented as a continuous line in Fig. 10. The best-fit values of the equivalent circuit elements from the CNLS fitting procedure are listed in Table II.

In general, the EIS responses of both types of hydrous oxide film were characterized by three relaxation processes. This is particularly clear from the three distinct capacitance peaks, modeled in order of decreasing frequency by the C_{film}, C_{dl}, and C_ϕ circuit elements, in the phase angle vs. log freq. Bode plots of Fig. 10. Equivalently, three pseudo-semi-circular regions can be discerned at lower potentials in the Nyquist plots of Fig. 10. Recently, Lyons and Brandon[38] reported a detailed discussion on the significance of the circuit model shown in Fig. 11 for passive oxide covered Ni, Co and Fe electrodes. The $C_{film}R_{film}$ loop of the equivalent circuit model is attributed to the dielectric properties and the resistivity of the underlying compact oxide film, respectively. The C_{dl} element models the double-layer capacitance, while R_Ω represents the uncompensated electrolyte resistance.
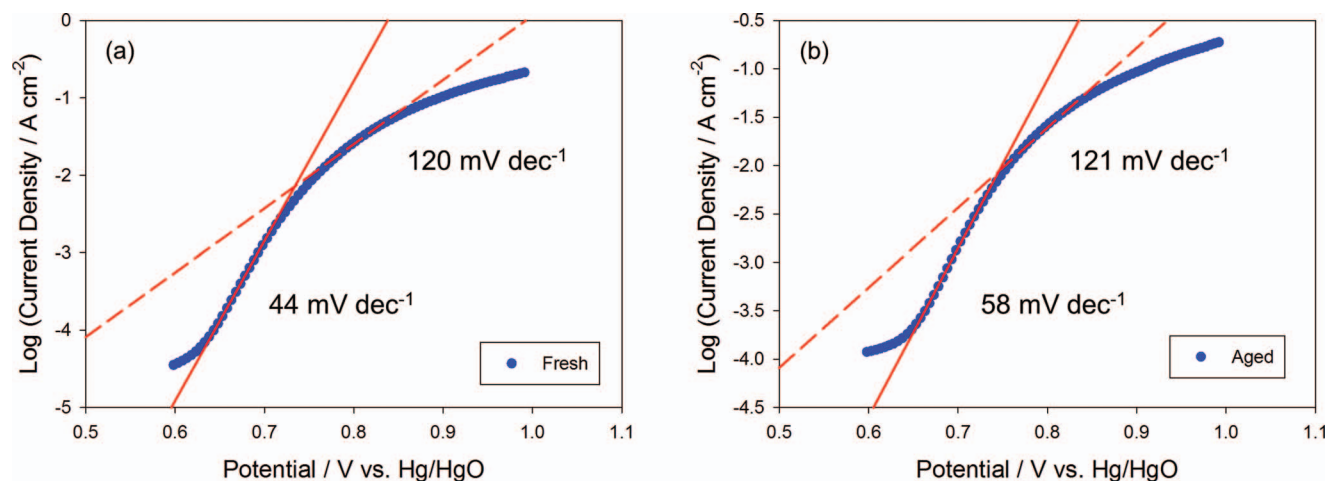
Figure 9. Steady-state polarization curves recorded in 5.0 mol dm^{-3} NaOH for a hydrous iron oxide film (a) before and (b) after immersing the film for 2 hours in 5.0 mol dm^{-3} NaOH. The film was grown using 120 growth cycles in 0.1 mol dm^{-3} NaOH between −1.33 V and 0.75 V at 400 mV s^{-1}.
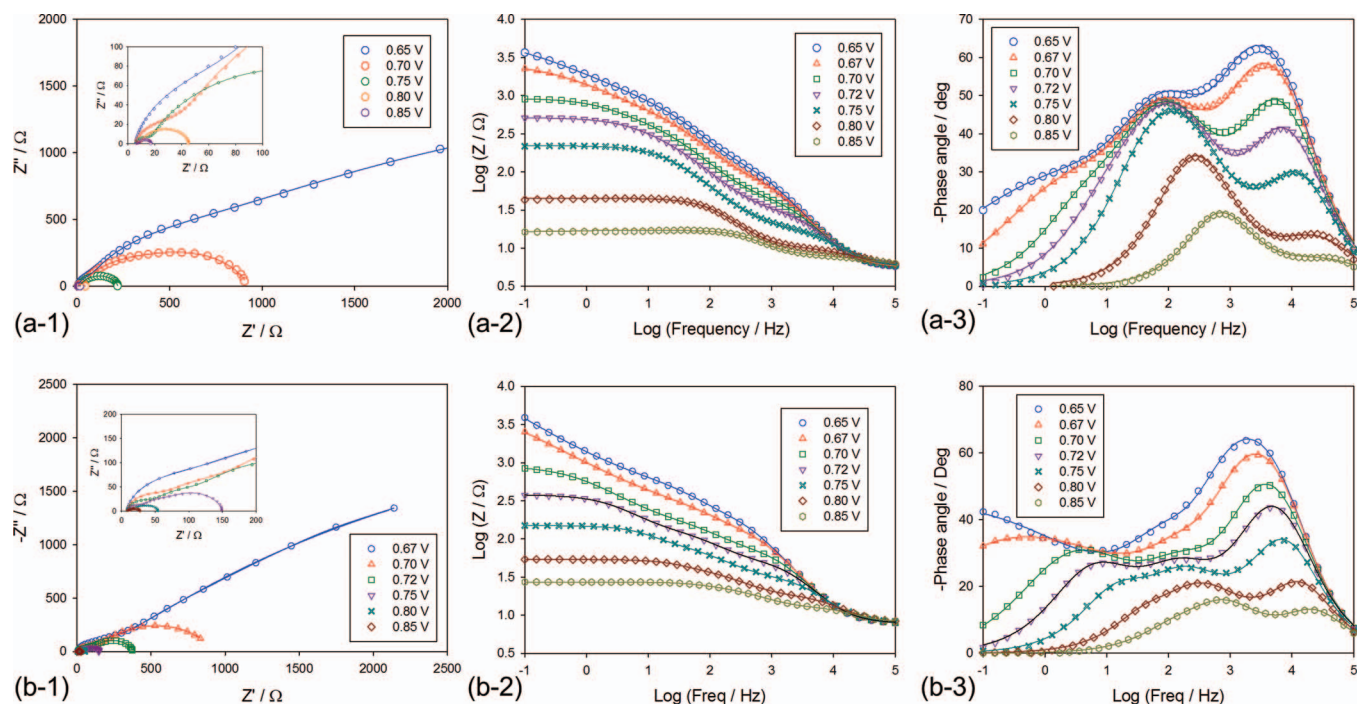

Figure 10. Electrochemical impedance spectra recorded in 1.0 mol dm^{-3} NaOH at a series of potentials associated with active oxygen evolution for (a) Type A and (b) Type B 120 cycled hydrous iron oxide films in the Nyquist[1] and Bode[2,3] format. The experiment data is represented by discrete points and the simulated impedance response is represented by a continuous line. The high frequency region of the Nyquist plot is shown as an inset.

Table II. Optimum fit parameters for the CNLS fitting of the impedance data in Fig. 10 to the equivalent circuit.

	Type A						Type B					
E / V	C_{film} /μF cm^{-2}	R_{film} / Ω	C_{dl} /μF cm^{-2}	R_p / Ω	C_ϕ / μF cm^{-2}	R_s / Ω	C_{film} /μF cm^{-2}	R_{film} / Ω	C_{dl} /μF cm^{-2}	R_p / Ω	C_ϕ / μF cm^{-2}	R_s / Ω
0.65	16.1	69.9	44.9	347.0	13.4	13420	14.9	144.1	44.3	237.1	41.6	32080
0.67	16.2	46.0	53.0	449.2	41.8	2328	14.6	90.4	46.7	122.5	59.7	7608
0.70	15.8	25.2	76.0	338.1	304.3	286.5	15.5	46.0	54.8	99.9	185.6	785.8
0.72	15.4	17.7	100.6	171.7	244.4	125.1	14.7	36.3	87.1	77.6	392.2	247.7
0.75	15.1	10.0	130.8	58.4	150.0	53.7	14.2	22.3	116.1	37.3	516.5	72.8
0.80	14.7	4.1	145.8	11.5	176.4	15.5	13.8	11.1	140.1	15.1	649.4	18.2
0.85	15.5	2.1	129.6	4.4	206.1	6.3	14.2	5.7	143.4	7.9	930.6	6.2

Note: Mean α values for C_{film}(0.95, 0.93), C_{dl}(0.88, 0.89) and C_ϕ(0.78, 0.78) for Type A and Type B films respectively.
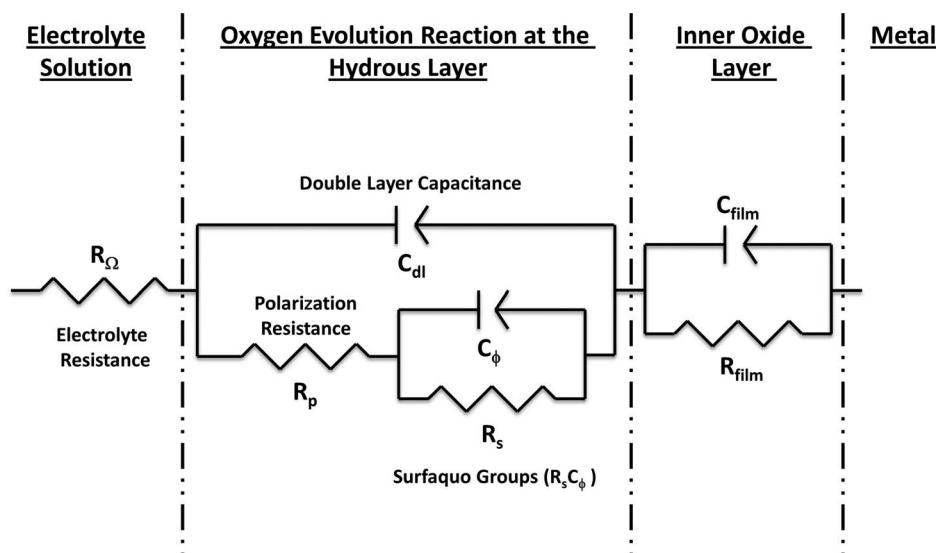
Figure 11. Equivalent circuit used in the CNLS fitting of the impedance data presented in Fig. 6.

The resistive elements R_s and R_p are related to the kinetics of the interfacial charge transfer reaction. In accordance with the work of Harrington and Conway,[39] R_p and R_s cannot be interpreted simply as the charge transfer resistances of the electrosorption and electrodesorption steps, respectively, but are each instead attributed to the properties of two or more steps in the overall reaction. Following the assertions of the same authors, C_ϕ is given the value of a capacitor which in parallel with R_s correctly models the relaxation of the charge associated with a surface intermediate. While it is tempting to interpret C_ϕ as the steady-state adsorption pseudo-capacitance,[40] Harrington and Conway[39] have shown that, in the general case, there is no simple relationship between these two quantities.

One further point regarding the equivalent circuit analysis was the necessity to use constant phase elements in place of pure capacitors. CPEs are commonly used to simulate frequency dispersion in the various capacitive responses of a system. Such frequency dispersion which is evident from the depressed nature of the semicircles in the Nyquist plots in Fig. 10 is believed to arise from surface roughness and inhomogeneity.[41] The impedance Z_{CPE} of a capacitive process displaying frequency dispersion is expressed as,

$$Z_{CPE} = A (j\omega)^{-\alpha} \qquad [5]$$

where $A = 1/C_{a=1}$, $C_{a=1}$ is the value of the capacitance in the absence of frequency dispersion and α is an exponent equal to unity for an ideal capacitor and $\alpha \leq 1$ for all other physically reasonable situations. The

result of a CNLS fitting of the raw impedance data to a CPE using the Thales SIM program, is an output in the form of optimized values for $C_{\alpha=1}$ and α. While the physical significance of the α parameter is uncertain, it is reasonable to conclude that the smaller the value of α the less uniform the electrode surface. Therefore, with increasing surface roughness and dispersion, the magnitude of α will decrease as the classical concept of the double layer capacitance of an ideally smooth uniform electrode/solution interface becomes progressively less applicable. Taking this into consideration, the average α values listed in Table II for C_{dl} and C_ϕ suggest that the hydrous oxide layer exhibits significant surface roughness.

In the present discussion, our primary interest is in the contrasting OER kinetic properties of Type A and Type B hydrous oxide films. Although both types of hydrous oxide film exhibit a similar general EIS response, characterized by three relaxation processes, distinct differences in their responses can also be observed in Fig. 10. In Fig. 12 a comparison of the impedance spectra for a Type A and Type B film at 0.70 V is presented in both the Nyquist and Bode format. It is clear that the high frequency impedance response is relatively unaffected by the film preparation method. This is further illustrated in Fig. 13 where it should be noted that similar fitting values were obtained for the C_{film} and R_{film} elements in the equivalent circuit model at each applied potential. These observations support our assignment of C_{film} and R_{film} as the capacitance and resistance, respectively, of the underlying compact oxide layer. The redox peaks
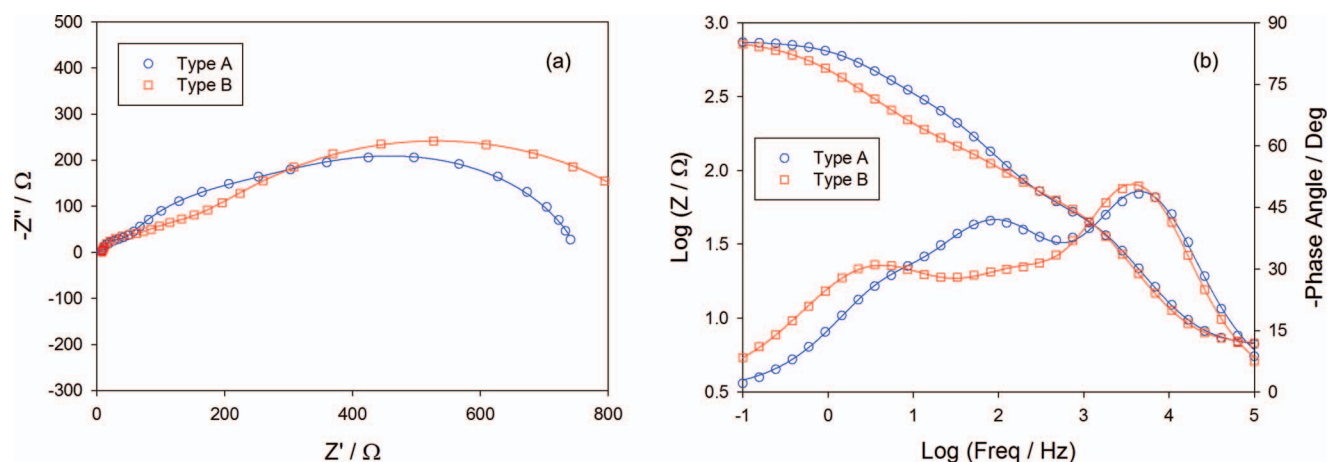

Figure 12. Electrochemical impedance spectra recorded at 0.70 V in 1.0 mol dm^{-3} NaOH for Type A and Type B hydrous oxide films represented in (a) Nyquist and (b) Bode format.
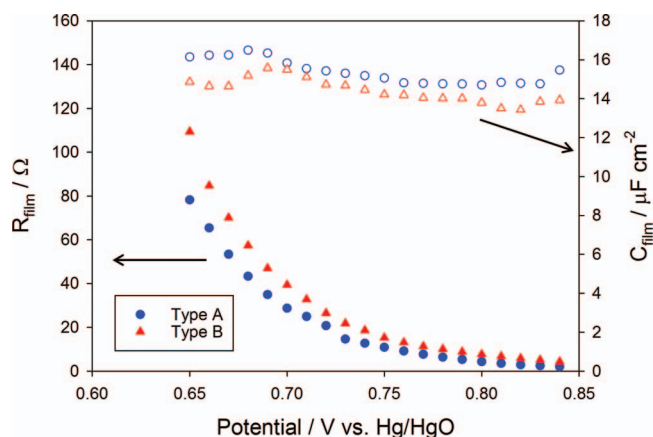
Figure 13. The optimum fitting values of C_{film} (blank data points) and R_{film} (filled data points) plotted as a function of applied potential for Type A and Type B 120 cycled hydrous oxide films.

attributed to the compact layer typically show little development with potential cycling and so, the film preparation method should not affect the properties of this layer. Conversely, the impedance responses at low to intermediate frequencies in Fig. 12 differ quite significantly with preparation method. Given that the impedance response at these frequencies is governed by the faradaic OER and that it is the outer hydrous layer and not the inner compact layer that will be affected by the growth conditions, this observation confirms our previous assertion that the OER catalytic centers are part of the hydrous layer. One further important conclusion which may be drawn from Fig. 13 is that the 'chemi-conductor' model outlined by Cahan and Chen,[42,43] in which the OER kinetics are masked by a highly resistive oxide film, does not apply to our system. This is evident from the relatively low film resistances obtained from the equivalent circuit analysis. Indeed, as can be seen in Fig. 13, a highly conducting film forms as the applied potential is increased. Therefore, we can assert that the low frequency impedance response is a true reflexion of the OER kinetics and not simply due to the changing conductivity of a highly resistive oxide film.

Taking this into consideration, we now conduct a closer examination of the individual contributions to the overall faradaic impedance in order to gain a better understanding of the different kinetic properties of the hydrous oxide films. The fitting values obtained for the $C_{dl}R_p$ and $C_{\phi}R_s$ loops in the equivalent circuit model are plotted as a function of applied potential in Fig. 14 and Fig. 15 respectively. Similar plots were obtained for hydrous oxide films prepared using

a range of growth cycles however no clear relationship between the redox charge capacity Q and the fitting values could be discerned. This is likely a result of the rather amorphous and nebulous nature of the hydrous oxide layer. In light of this, we restrict our analysis here to Type A and Type B films prepared using 120 growth cycles. It is clear from Fig. 14a that both films exhibit similar double-layer capacitive behavior. For ease of discussion the OER steady-state current is also shown. Initially, before the onset of significant oxygen evolution current, the value of C_{dl} was approximately 44 μF cm^{-2}. This elevated value of C_{dl}, in comparison with a typical double-layer capacitance, is to be expected given the oxide covered nature of the electrode surface. Indeed the average α value shown in Table II for the C_{dl} element was 0.88 indicating significant roughness of the electrode surface. As the applied potential was increased, the value of C_{dl} also increased up to an apparent maximum. Interestingly, the increase in the capacitance coincided with the onset of significant oxygen evolution current. Therefore, this variation in the value of C_{dl} is likely a reflexion of the increasing concentration of charged surface states as the OER progresses. However, the origin of the capacitive maximum is uncertain. That said, Bisquert and coworkers[44] have observed a similar trend for IrO_2 and IrO_2/Nb_2O_5 electrodes. The latter authors attributed the observed maximum and subsequent decrease in the capacitance to the strong evolution of gas bubbles at the higher potentials. This could reduce in total the exposed surface area of the electrode thereby influencing its capacitive behavior.

The polarization resistance R_p can be viewed as a total charge transfer resistance for the combined steps of the OER. In the theoretical treatment of Harrington and Conway[39] the reciprocal resistance $1/R_p$ was shown to be equal to the sum of similar reciprocal resistances for each of the individual charge transfer steps. Consequently, R_p is related to the overall rate of the OER. The variation of R_p as a function of applied potential is presented in Fig. 14b. As expected for a faradaic process, the resistance for each film decreases with increasing potential indicating increased electron transfer kinetics. At high potentials, $E \geq 0.76$ V, there is little difference in the R_p values obtained for each film. However, at lower potentials the resistances diverge with Type A films displaying significantly greater R_p values than Type B films. Importantly, this observation mirrors the Tafel characteristics associated with these films. Recall that all the hydrous oxide films exhibit 120 mV dec^{-1} Tafel slopes at high overpotentials whereas at low overpotentials the Tafel slopes deviate, giving 60 mV dec^{-1} and 40 mV dec^{-1} slopes for the Type A and Type B films respectively. In fact, the potential around which the resistances deviate is located in the low to high Tafel slope transition region, as can be observed from Fig. 6. In this way, the lower R_p values obtained for Type B films at low overpotentials are consistent with the idea that a lower Tafel slope corresponds with improved electrocatalytic properties.
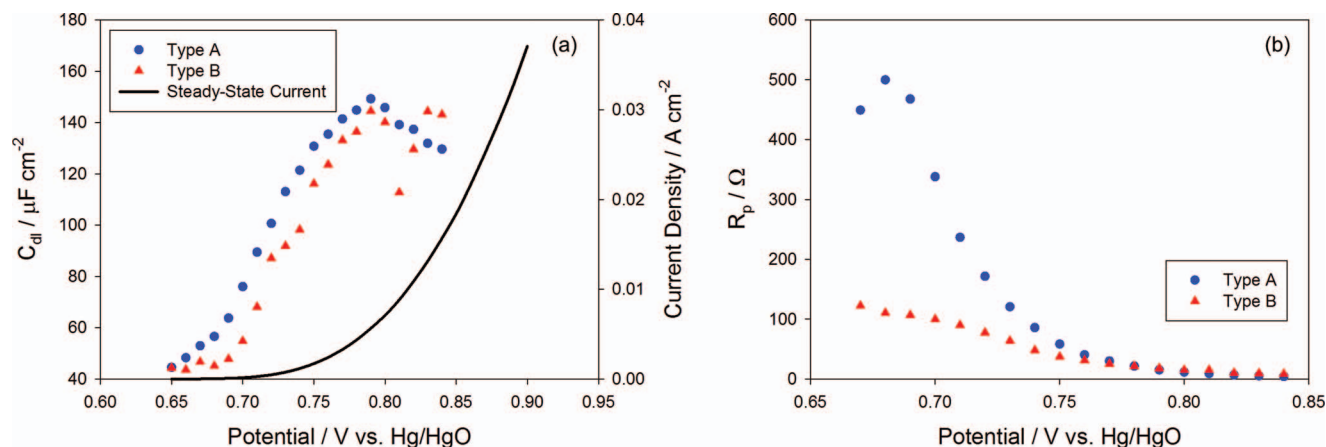

Figure 14. The optimum fitting values of (a) C_{dl} and (b) R_p plotted as a function of applied potential for Type A and Type B 120 cycled hydrous oxide films. A typical steady state current profile for a 120 cycled Type A film is also presented in (a) above.
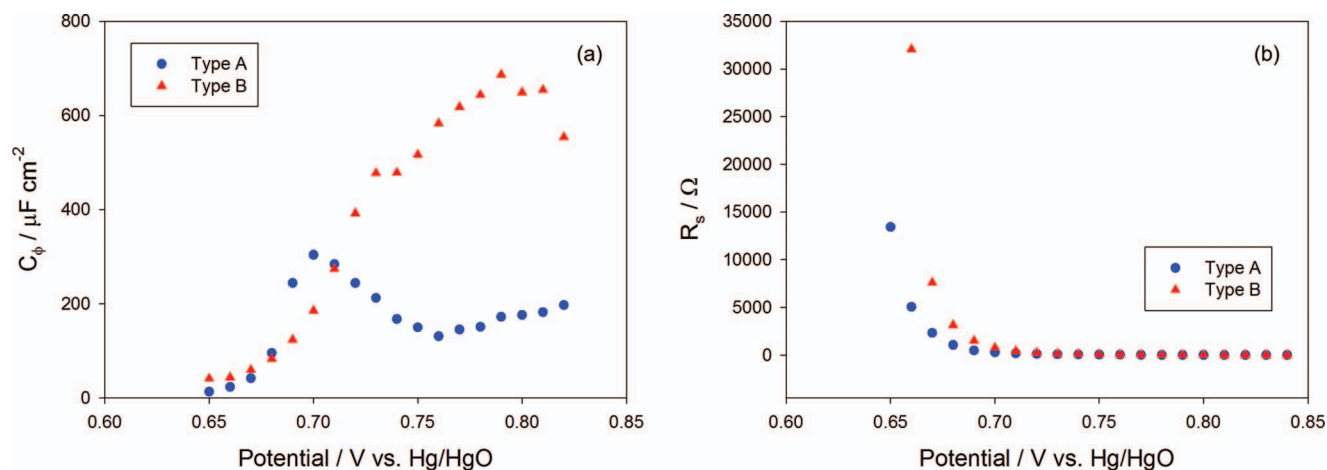
Figure 15. The optimum fitting values of (a) C_ϕ and (b) R_s plotted as a function of applied potential for Type A and Type B 120 cycled hydrous oxide films.

In Fig. 15 the variation of C_ϕ and R_s with potential can be observed for both types of hydrous oxide film. It has been noted previously that the $C_\phi R_s$ loop in the equivalent circuit models the relaxation of charge associated with a surface intermediate. In this sense, C_ϕ can be related to the changing concentration of charged intermediates as the OER progresses. It is clear from Fig. 15a that C_ϕ increased with applied potential eventually reaching a maximum for both films. Such a trend might be expected for a capacitance arising from a faradaic process. However, the magnitude and potential at which these maxima occur differs greatly for each film. The maximum C_ϕ value is significantly smaller for Type A films and occurs approximately 100 mV less anodic than that for the Type B film. This can also be observed on a more qualitative level from the Bode-phase plots in Fig. 10 where we note that the low frequency capacitance maximum attributed to C_ϕ is more readily distinguishable for the Type B films. Although the physical reason behind this is unknown, the fact that these two trends are at variance with each other suggests that the C_ϕ element describes a different charging process for each film. That is, the intermediates involved in the rate determining process are not the same for each type of film, in agreement with the contrasting Tafel behavior observed for Type A and Type B hydrous oxide films.

In a similar manner, the divergent behavior of Rs is also reflective of the differing Tafel characteristics of the hydrous oxide films. It can be seen from Fig. 15b that the R_s values decrease significantly with applied potential. Moreover, as was the case for R_p, these values differ greatly at low potentials. Harrington and Conway[39] have shown that R_s is related, albeit in a rather complicated fashion, to the rate of production of one or more surface intermediates. In a general way, R_s gives an indication of the ease with which these species can be formed. Thus, as the potential is increased, the intermediate is more readily formed and R_s decreases. Accordingly, it is fitting that R_s diverges for Type A and Type B films at potentials corresponding to the low Tafel region as this is a further illustration of the change in the rate determining step associated with these films.

Finally, we perform a Tafel analysis of the OER impedance data. EIS provides a useful accessory method for the determination of Tafel slopes, especially when combined with dc steady state polarization data. Obtaining equivalent Tafel slopes using EIS involves the experimental determination of the total faradaic resistance R_{far} as a function of applied potential. In the present case, R_{far} is calculated from the fitting parameters as $R_{far} = R_p + R_s$. At an oxygen evolution overpotential η where simple Tafel behavior prevails, the current density i is related to η *via* the following expression,

$$i = i_0 \exp\left(2.303\eta/b\right) \qquad [6]$$

where i_0 is the exchange current density for the OER. Taking the derivative of i with respect to η gives,

$$\frac{di}{d\eta} = \frac{2.303i}{b} \exp\left(2.303\eta/b\right) \qquad [7]$$

Therefore, noting that $di/d\eta = di/dE = 1/R_{far}$, and by performing a logarithmic analysis of eqn. 7 the following expression is achieved,
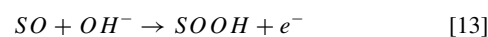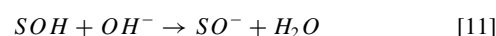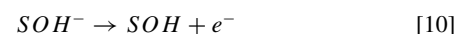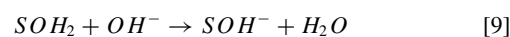
$$\log\left(\frac{1}{R_{far}}\right) = \frac{E}{b} + \log\left(\frac{2.303i_0}{b}\right) \qquad [8]$$

implying that the inverse slope of a plot of $\log(1/R_{far})$ against E is equal to the Tafel slope b.

The plots of $\log(1/R_{far})$ vs. E generated for the 120-cycled Type A and Type B hydrous oxide films are presented in Fig. 16. For ease of comparison, the corresponding dc Tafel plots are also shown. It is apparent that there is excellent agreement between the two different methods. Tafel slopes of ca. 60 mV dec^{-1} and 40 mV dec^{-1} were observed at low overpotentials for the Type A and Type B films respectively with a Tafel slope of ca. 120 mV dec^{-1} uniformly observed at high overpotentials, for both the steady state polarization data and the impedance data.

Mechanism of oxygen evolution.— In summary, any mechanistic interpretation of the OER at multi-cycled Fe electrodes must be capable of accounting for the variety of kinetic parameters outlined above. To aid in our mechanistic discussion these parameters have been summarized in Table III. For the purposes of a theoretical analysis we have assumed idealized values for each reaction order and these are shown in parentheses in Table III.

Our proposed mechanism is represented schematically in Scheme A and can also be described by the following reaction sequence,
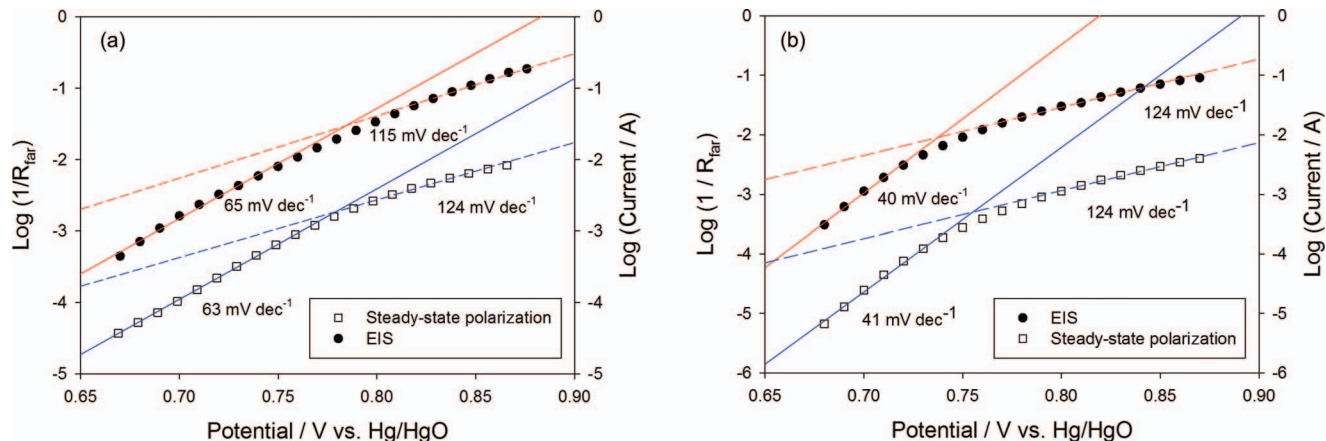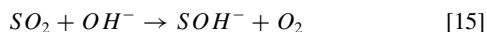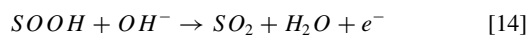
$$SOH_2 + OH^- \rightarrow SOH^- + H_2O \qquad [9]$$

$$SOH^- \rightarrow SOH + e^- \qquad [10]$$

$$SOH + OH^- \rightarrow SO^- + H_2O \qquad [11]$$

$$SO^- \rightarrow SO + e^- \qquad [12]$$

$$SO + OH^- \rightarrow SOOH + e^- \qquad [13]$$

Figure 16. Tafel plots generated from EIS and Steady-state polarization data recorded in 1.0 mol dm^{-3} NaOH for (a) Type A and (b) Type B 120 cycled hydrous oxide films.

$$SOOH + OH^- \rightarrow SO_2 + H_2O + e^- \qquad [14]$$

$$SO_2 + OH^- \rightarrow SOH^- + O_2 \qquad [15]$$

where S represents a surfaquo group attached to the hydrous oxide surface by bridging oxygen ligands. Note that octahedrally co-ordinated oxy-iron surfaquo groups are identified as the catalytically active species and are located within the hydrous layer. This mechanism takes advantage of the fact that the dispersed hydrous layer contains considerable quantities of water molecules which facilitate hydroxide ion discharge at the metal catalytic site. In this way our mechanistic thinking is guided by the earlier work of Kobussen and Broers,[27] but also takes into account recent developments in DFT calculations[45,46] and homogeneous OER catalysis.[47–49]

We now conduct a comprehensive kinetic analysis of the mechanism outlined in Scheme A. First, we note that the first step in the reaction sequence occurs rapidly and need not be included in the steady-state kinetic analysis. Therefore, if we assume that the step outlined in eqn. 11 is rate determining then the net reaction flux is given by,

$$f_\Sigma = i/4FA = k_2 a_{OH^-} \Gamma_{SOH} \qquad [16]$$

In the latter expression a_{OH^-} represents the activity of the hydroxyl ion and Γ denotes the surface coverage. We use the quasi steady-state approximation for the surface coverage of SOH to get,

$$\frac{d\Gamma_{SOH}}{dt} = k'_1 \Gamma_{SOH^-} - k'_{-1} \Gamma_{SOH} - k_2 \Gamma_{SOH} a_{OH^-} \cong 0 \qquad [17]$$

which we may readily solve to obtain an expression for the surface coverage,

$$\Gamma_{SOH} \cong k'_1 \Gamma_{SOH^-} / \left(k'_{-1} + k_2 a_{OH^-} \right) \qquad [18]$$

Hence the net flux is given by,

$$f_\Sigma \cong \frac{k_2 k'_1 a_{OH^-} \Gamma_{SOH^-}}{k'_{-1} + k_2 a_{OH^-}} \qquad [19]$$

In the latter expression the primed quantities represent heterogeneous electrochemical rate constants whose potential dependence is assumed to be given by the Butler-Volmer rate equation,

$$k'_n = k^0_n \exp\left(\frac{\beta F \eta}{RT}\right), k'_{-n} = k^0_{-n} \exp\left(\frac{-(1-\beta) F \eta}{RT}\right) \qquad [20]$$

where η denotes the overpotential and β is the symmetry factor. In contrast the chemical rate constant is given by its standard value and there is no potential dependence,

$$k_n = k^0_n \qquad [21]$$

Hence the net flux is given by,

$$f_\Sigma \cong \frac{k^0_2 a_{OH^-} \Gamma_{SOH^-} k^0_1 \exp\left[\beta F \eta / RT\right]}{k^0_{-1} \exp\left[-(1-\beta) F \eta / RT\right] + k^0_2 a_{OH^-}} \qquad [22]$$

Now if the step outlined in eqn. 11 is rate determining then we can safely assume that $k^0_2 \ll k^0_{-1}$ and so eqn. 22 reduces to,

$$f_\Sigma \cong k^0_2 \Gamma_{SOH^-} a_{OH^-} \left(k^0_1 / k^0_{-1}\right) \exp\left[F \eta / RT\right] \qquad [23]$$

This expression can be readily shown to predict a reaction order of unity with respect to hydroxide ion activity and a Tafel slope at 298 K of ca. 60 mV dec^{-1} ($b = 2.303(RT/F)$).

However, if the subsequent step outlined in eqn. 12 becomes rate limiting we can write that,

$$f_\Sigma \cong k'_3 \Gamma_{SO^-} \qquad [24]$$

Again applying the quasi steady-state approximation we can show that,

$$\frac{d\Gamma_{SO^-}}{dt} = k_2 \Gamma_{SOH} a_{OH^-} - k_{-2} a_{H_2O} \Gamma_{SO^-} - k'_3 \Gamma_{SO^-} \cong 0 \qquad [25]$$

Table III. Experimentally determined kinetic parameters for the OER at hydrous iron oxide covered electrodes.

	Low Tafel Region		High Tafel Region	
Growth Medium / mol dm^{-3}	b / mV dec^{-1}	m_{OH^-}	b / mV dec^{-1}	m_{OH^-}
0.1	40 (2Γ/3)	0.98 (1.0)	120 (2Γ)	0.62 (0.5)
0.5	40 (2Γ/3)	1.41 (1.5)	120 (2Γ)	0.91 (1.0)
1.0	60 (Γ)	1.04 (1.0)	120 (2Γ)	0.94 (1.0)
5.0	60 (Γ)	0.92 (1.0)	120 (2Γ)	0.77 (1.0)

Note: Theoretical diagnostic values are given in parentheses where $\Gamma = 2.303RT/F$. Growth medium was aqueous NaOH.
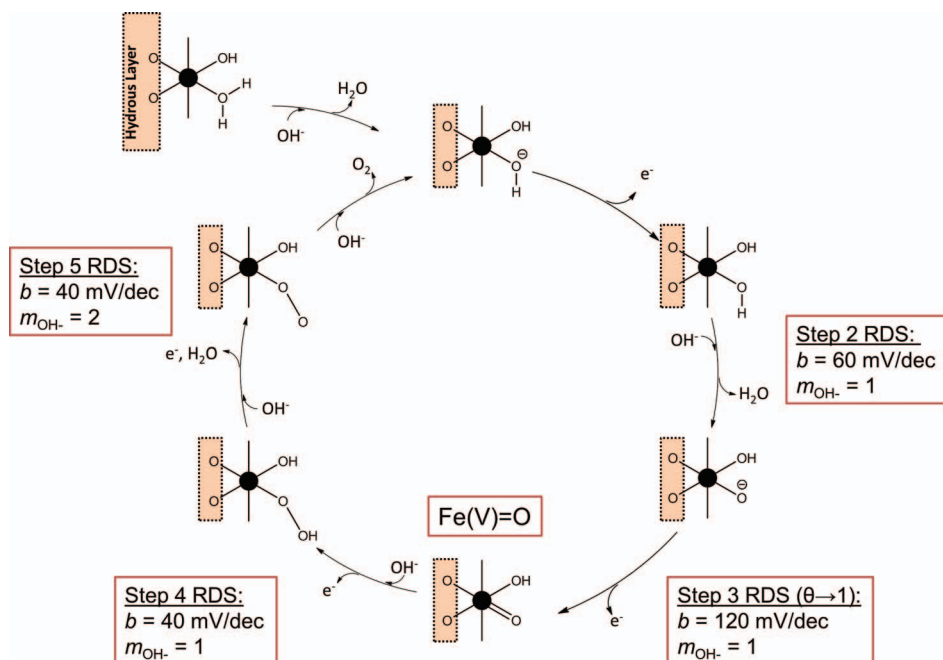
Scheme A. Mechanism for the OER involving octahedrally coordinated Fe oxyhydroxide surfaquo group.

and solving for the surfaquo group coverage we obtain,

$$\Gamma_{SO^-} \cong k_2^0 \Gamma_{SOH} a_{OH^-} / \left(k_{-2}^0 a_{H_2O} + k_3^0 \exp\left[\beta F\eta/RT\right]\right) \qquad [26]$$

Hence the net reaction flux is given by,

$$f_\Sigma \cong \frac{k_2^0 k_3^0 a_{OH^-} \Gamma_{SOH} \exp\left[\beta F\eta/RT\right]}{k_{-2}^0 a_{H_2O} + k_3^0 \exp\left[\beta F\eta/RT\right]} \qquad [27]$$

Now at high overpotentials it is reasonable to assume that $\Gamma_{SOH} \cong 1$ and also $k_{-2}^0 \gg k_3^0$. Thus, we obtain that,

$$f_\Sigma \cong k_3^0 a_{H_2O}^{-1} \left(k_2^0/k_{-2}^0\right) a_{OH^-} \exp\left[\beta F\eta/RT\right] \qquad [28]$$

Hence, when the electrochemical oxo generation step eqn. 12 is rate limiting at high overpotentials the flux expression presented in eqn. 28 predicts that a reaction order of unity with respect to hydroxide ion activity and a Tafel slope of ca. 120 mV dec^{-1} at 298 K ($b = 2.303(2RT/F)$) will be observed assuming that $\beta = 1/2$.

Using a similar approach it can be shown that our mechanism predicts a Tafel slope of ca. 40 mV dec^{-1} at 298 K ($b = 2.303(2RT/3F)$) with corresponding reaction orders of unity and 2, respectively, if the formation of the metal peroxide $SOOH$ or the metal peroxo SOO species are assumed to be rate determining. While it should be noted from Table III that neither of these steps directly account for the low overpotential kinetic parameters associated with the hydrous oxide films prepared in 0.5 mol dm^{-3} NaOH, Trasatti and coworkers[50] have proposed that fractional reaction orders can be attributed to competing reaction pathways. In such cases, the latter authors suggest the experimentally observed kinetic parameters represent a combination of the parameters expected for the competing pathways, the exact value of which depends on the fraction of catalytic sites following each individual pathway. Following this logic, if we assume that the steps involving the formation of the $SOOH$ and SOO species are both equally rate limiting then, applying the steady-state kinetic analysis outlined above, a reaction order of ca. 1.5 may be predicted with an associated Tafel slope of ca. 40 mV dec^{-1}. Therefore, it is gratifying to note that our current mechanism is in excellent agreement with the available kinetic data. That said, further analysis is required to fully account for the kinetic parameters observed at high overpotentials for the hydrous oxide films prepared in 0.1 mol dm^{-3} NaOH.

In view of the above kinetic analysis, we wish to highlight here a number of important features of our current mechanism. Firstly, it is important to note that our proposed catalytic cycle for the OER

outlined in Scheme A is analogous to those depicted for various homogeneous catalyst systems.[47–49] This is not unexpected given the very dispersed and somewhat tenuous nature of the catalytically active hydrous oxide layer. A common feature of these reaction schemes is that the initial catalytic step involves the deprotonation of a metal coordinated water molecule. However, in the strongly alkaline conditions used in this system it is likely that a significant proportion of these coordinated water molecules will already be deprotonated. The pK$_a$ value for a water molecule coordinated to a highly charged metal atom is generally in the range pK$_a$ 5-9.[51] In light of this, it is more reasonable to assume that the initial deprotonation step is facile and will occur outside of the catalytic cycle. Hence, the initial deprotonation step is depicted as a pre-step in Scheme A and the OER catalytic cycle begins with the resultant coordinated OH$^-$ ion which we label SOH^-.

Secondly, it is clear that one of the key steps in our proposed mechanism involves the formation of a surface bound metal oxo SO species. In scheme A above this species is depicted as M = O suggesting an M(V) metal center. However, this species could also be represented as a metal oxyl moiety M(IV)-O·. In actual fact, the degree of radical character has been shown to depend on the length of the metal oxo bond with M(V) = O being more stable for shorter bond lengths.[47,52] In the case of Fe, it is likely that the metal oxo species involves an Fe(V) metal center. Indeed, a recent variable temperature mass spectrometry investigation has identified an Fe(V) oxo species as the catalytic center in a biomimetric non-heme Fe complex.[53]

Finally, we note that the formation of metal oxide SO^- eqn. 11, metal oxo SO eqn. 12 and metal peroxide $SOOH$ eqn. 13 species have been designated as possible rate determining steps in Scheme A. To date, atomic-scale insight into the OER has proven difficult due to the lack of significant spectroscopic evidence of intermediates. However, recent surface-enhanced Raman spectroscopy (SERS) studies provide convincing evidence for $SOOH$ intermediates on Au, Ni and Co substrates.[54–56] Specifically, Bell and coworkers[55] found that a characteristic v(O-O) band of quite low intensity at 815–830 cm^{-1} could only be observed for a Au substrate at potentials associated with active oxygen evolution. Indeed, the low intensity of the v(O-O) band in this study highlights the difficulty in obtaining direct experimental evidence for OER intermediates. On the other hand, Muckermann and coworkers propose,[46] based on DFT calculations, that for a GaN/ZnO surface with high coverage of adsorbed OH$^-$ ions the intermediate associated with the highest energy is an oxide

radical. Similarly, Rossmeisl et al.[45] performed DFT studies on the OER at RuO_2 surfaces. They too found that for a surface saturated with adsorbed OH, the highest energy intermediate was a surface oxygen species, in this case an oxo species. Furthermore, the latter authors assigned the highest energy state to a peroxide intermediate when the surface was saturated with adsorbed oxo rather than hydroxide species. Therefore, considering these studies, the present mechanistic interpretation brings together a number of strands in the current understanding of the OER at metal oxide electrodes, and reflects current thinking in the allied field of water oxidation in homogeneous catalytic systems *via* transition metal complexes.

Conclusions

In conclusion, we have described the growth of hydrous iron oxyhydroxide films on iron substrates in aqueous base and examined the kinetics of active oxygen evolution at these electrodes. Steady-state Tafel plots and electrochemical impedance spectroscopy have been shown to complement each other to provide an effective kinetic analysis of the OER at multicycled iron electrodes. The hydrous oxide films are easy to prepare and the factors affecting their growth and electrocatalytic properties have been described in detail. Moreover, the acid/base behavior of the anodically prepared films is an important factor to take into account when considering the mechanism of oxygen evolution.

A novel mechanism involving the active participation of iron oxyhydroxide surfaquo groups has been developed. This mechanism, which is in excellent agreement with experimental data, is inspired by the classic work of Kobussen and Broers[27] while also resonating with more recent work concerning various oxygen evolving molecular inorganic transition metal complexes.[47–49,52] In our mechanistic interpretation we consider the microdispersed layer as an elongated intermingled array of octahedrally coordinated Fe surfaquo groups. Importantly, the structure of the surfaquo groups mirrors that of homogeneous molecular catalysts. Furthermore, with support from recent spectroscopic and DFT data, iron oxide, oxo and peroxide species are proposed as important intermediates in the oxygen evolution reaction under electrochemical conditions. Thus, in our work we have integrated the allied fields of heterogeneous and homogeneous OER catalysis. Indeed, we can conclude that the chemistry of the surfaquo group determines the chemistry of the OER catalytic cycle.

Acknowledgments

References

1. K. Zeng and D. Zhang, *Prog. Energy Combust. Sci.*, **36**, 307 (2010).
2. H. Tributsch, *Int. J. Hydrogen Energy*, **33**, 5911 (2008).
3. G. W. Crabtree, M. S. Dresselhaus, and M. V. Buchanan, *Phys. Today*, December, 39 (2004).
4. J. Ohi, *J. Mater. Res.*, **20**, 3180 (2005).
5. D. E. Hall, *J. Electrochem. Soc.*, **130**, 317 (1983).
6. A. Michas, F. Andolfatto, M. E. G. Lyons, and R. Durand, *Key Eng. Mater.*, **72-74**, 535 (1992).
7. K. Kinoshita, *Electrochemical Oxygen Technology*, Wiley-Interscience, New York (1992).
8. M. E. G. Lyons and M. P. Brandon, *Int. J. Electrochem. Sci.*, **3**, 1386 (2008).
9. M. E. G. Lyons and M. P. Brandon, *Int. J. Electrochem. Sci.*, **3**, 1425 (2008).
10. M. E. G. Lyons and M. P. Brandon, *Int. J. Electrochem. Sci.*, **3**, 1463 (2008).
11. M. E. G. Lyons, R. L. Doyle, and M. P. Brandon, *Phys. Chem. Chem. Phys.*, **13**, 21530 (2011).
12. M. E. G. Lyons, L. Russell, M. O'Brien, R. L. Doyle, I. Godwin, and M. P. Brandon, *Int. J. Electrochem. Sci.*, **7**, 2710 (2012).
13. M. Plata-Torres, A. M. Torres-Huerta, M. A. Dominguez-Crespo, E. M. Arce-Estrada, and C. Ramirez-Rodriguez, *Int. J. Hydrogen Energy*, **32**, 4142 (2007).
14. R. N. Singh, J. P. Pandey, and K. L. Anitha, *Int. J. Hydrogen Energy*, **18**, 467 (1993).
15. M. Kumar, R. Awasthi, A. K. Pramanick, and R. N. Singh, *Int. J. Hydrogen Energy*, **36**, 12698 (2011).
16. M. Garcia-Mota, A. Vojvodic, H. Metiu, I. C. Man, H.-Y. Su, J. Rossmeisl, and J. K. Norskov, *Chem. Cat. Chem.*, **3**, 1607 (2011).
17. J. Suntivich, K. J. May, H. A. Gasteiger, J. B. Goodenough, and Y. Shao-Horn, *Science*, **334**, 1383 (2011).
18. J. O'M. Bockris and T. Otagawa, *J. Phys. Chem.*, **87**, 2960 (1983).
19. Y.-R. Hong, Z. Liu, S. F. Al-Bukhari, C. J. J. Lee, D. L. Yung, D. Chi, and T. S. A. Hor, *Chem. Comm.*, **47**, 10653 (2011).
20. K. G. Wijayantha, S. Saremi-Yarahmadi, and L. M. Peter, *Phys. Chem. Chem. Phys.*, **13**, 5264 (2011).
21. B. Klahr, S. Gimenez, F. Fabregat-Santiago, T. Hamann, and J. Bisquert, *J. Am. Chem. Soc.*, **134**, 4294 (2012).
22. M. E. G. Lyons and M. P. Brandon, *Phys. Chem. Chem. Phys.*, **11**, 2203 (2009).
23. M. E. G. Lyons and R. L. Doyle, *Int. J. Electrochem. Sci.*, **6**, 5710 (2011).
24. M. E. G. Lyons and L. D. Burke, *J. Electroanal. Chem.*, **170**, 377 (1984).
25. R. L. Doyle and M. E. G. Lyons, *Phys. Chem. Chem. Phys.*, in review.
26. R. F. Scarr, *J. Electrochem. Soc.*, **116**, 1526 (1969).
27. A. G. C. Kobussen and G. H. J. Broers, *J. Electroanal. Chem.*, **126**, 221 (1981).
28. L. D. Burke and M. E. G. Lyons, *J. Electroanal. Chem.*, **198**, 347 (1986).
29. L. D. Burke and D. P. Whelan, *J. Electroanal. Chem.*, **162**, 121 (1984).
30. L. D. Burke and E. J. M. O'Sullivan, *J. Electroanal. Chem.*, **117**, 155 (1981).
31. L. D. Burke, M. I. Casey, V. J. Cunnane, O. J. Murphy, and T. A. M. Twomey, *J. Electroanal. Chem.*, **189**, 353 (1985).
32. P. G. Pickup and V. I. Birss, *J. Electroanal. Chem.*, **220**, 83 (1987).
33. S. Rebouillat, M. E. G. Lyons, M. P. Brandon, and R. L. Doyle, *Int. J. Electrochem. Sci.*, **6**, 5830 (2011).
34. M. R. Gennero De Chialvo and A. C. Chialvo, *Electrochim. Acta*, **33**, 825 (1988).
35. M. R. Gennero De Chialvo and A. C. Chialvo, *Electrochim. Acta*, **35**, 437 (1990).
36. M. E. G. Lyons and R. L. Doyle, *Int. J. Electrochem. Sci.*, **7**, 9488 (2012).
37. R. A. Robinson and R. H. Stokes, *Electrolyte Solutions*, p. 492, Butterworth & Co. Ltd., London (1965).
38. M. E. G. Lyons and M. P. Brandon, *J. Electroanal. Chem.*, **631**, 62 (2009).
39. D. A. Harrington and B. E. Conway, *Electrochim. Acta*, **32**, 1703 (1987).
40. B. E. Conway and E. Gileadi, *Trans. Faraday Soc.*, **58**, 2493 (1962).
41. B. E. Conway, in *Impedance Spectroscopy—Theory, Experiment, and Applications*, E. Barsoukov and J. R. Macdonald, Editors, p. 469–497, J. Wiley & Sons, New Jersey (2005).
42. B. D. Cahan and C. T. Chen, *J. Electrochem. Soc.*, **129**, 700 (1982)
43. B. D. Cahan and C. T. Chen, *J. Electrochem. Soc.*, **129**, 921 (1982)
44. A. J. Terezo, J. Bisquert, E. C. Pereira, and G. Garcia-Belmonte, *J. Electroanal Chem.*, **508**, 59 (2001).
45. J. Rossmeisl, Z.-W. Qu, H. Zhu, G.-J. Kroes, and J. K. Norskov, *J. Electroanal. Chem.*, **607**, 83 (2007).
46. X. Shen, Y. A. Small, J. Wang, P. B. Allen, M. V. Fernandez-Serra, M. S. Hybertsen, and J. T. Muckerman, *J. Phys. Chem. C*, **114**, 13695 (2010).
47. M. Busch, E. Ahlberg, and I. Panas, *Phys. Chem. Chem. Phys.*, **13**, 15069 (2011).
48. L.-P. Wang, Qin Wu, and T. Van Voorhis, *Inorg. Chem.*, **49**, 4543 (2010).
49. L. Duan, F. Bozoglian, S. Mandal, B. Stewart, T. Privalov, A. Llobet, and L. Sun, *Nature*, **4**, 418 (2012).
50. A. Carugati, G. Lodi, and S. Trasatti, *Mater. Chem.*, **6**, 255 (1981).
51. G. A. Lawrence, *Introduction to Coordination Chemistry*, p. 199, J. Wiley & Sons, West Sussex (2010).
52. P. E. M. Siegbann and R. H. Crabtree, *J. Am. Chem. Soc.*, **121**, 117 (1999).
53. A. R. McDonald and L. Que, *Nature*, **3**, 761 (2011).
54. B. S. Yeo and A. T. Bell, *J. Am. Chem. Soc.*, **133**, 5587 (2011).
55. B. S. Yeo, S. L. Klaus, P. N. Ross, R. A. Mathies, and A. T. Bell, *Chem. Phys. Chem.*, **11**, 1854 (2010).
56. B. S. Yeo and A. T. Bell, *J. Phys. Chem. C*, **116**, 8394 (2012).